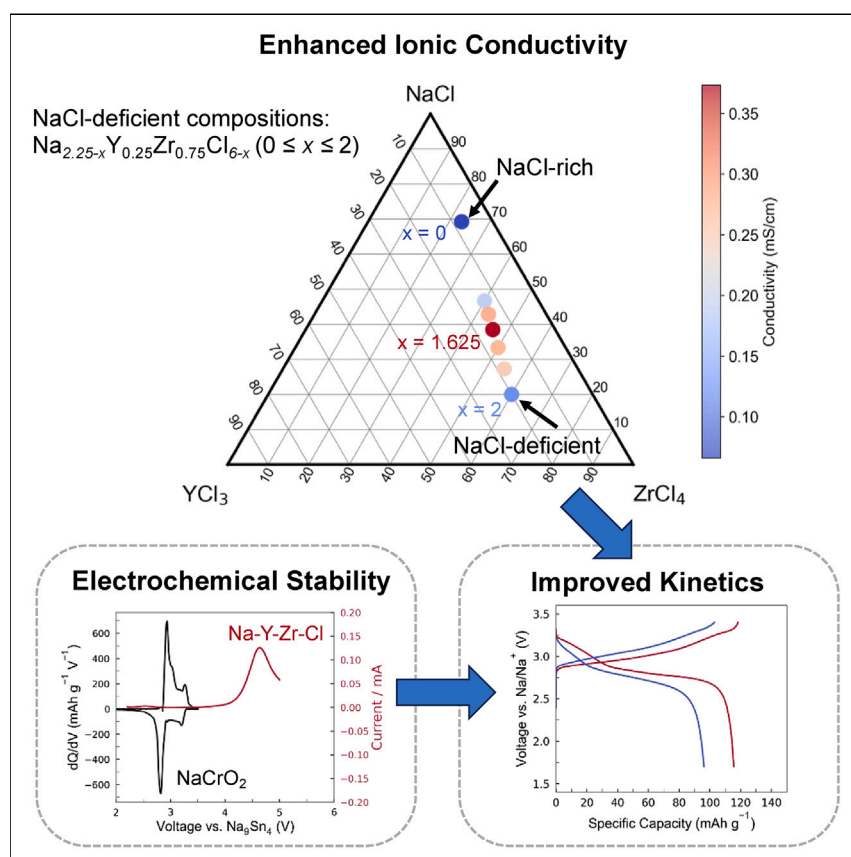


## Article

## Amorphous and nanocrystalline halide solid electrolytes with enhanced sodium-ion conductivity



Despite the potential for affordable, safe, and reliable energy storage offered by sodium solid-state batteries, hurdles remain concerning manufacturing and their performance at room temperature. Here, we explore the Na-Y-Zr-Cl compositional space and show that reduced NaCl molar content results in the formation of nanocrystalline and amorphous phases with enhanced ionic conductivity, thus improving ambient battery performance. These insights can be used to further enhance solid-state battery performance and to broaden the design space for chloride solid electrolytes.

Phillip Ridley, Long Hoang Bao Nguyen, Elias Sebti, ..., Raphaële Clément, Jihyun Jang, Ying Shirley Meng

jihyunjang@sogang.ac.kr (J.J.)  
 shirleymeng@uchicago.edu (Y.S.M.)

**Highlights**

NaCl-deficient Na-Y-Zr-Cl compositions form nanocrystalline and amorphous phases

Enhanced conductivity arises from reduced grain size and amorphous domains

Improved room temperature solid-state battery performance owed to superior conductivity

**Demonstrate**

Proof-of-concept of performance with intended application/response

## Article

# Amorphous and nanocrystalline halide solid electrolytes with enhanced sodium-ion conductivity

Phillip Ridley,<sup>1</sup> Long Hoang Bao Nguyen,<sup>1</sup> Elias Sebti,<sup>2</sup> Bing Han,<sup>1</sup> George Duong,<sup>1</sup> Yu-Ting Chen,<sup>3</sup> Baharak Sayahpour,<sup>3</sup> Ashley Cronk,<sup>3</sup> Grayson Deysher,<sup>3</sup> So-Yeon Ham,<sup>3</sup> Jin An Sam Oh,<sup>1</sup> Erik A. Wu,<sup>1</sup> Darren H.S. Tan,<sup>1</sup> Jean-Marie Doux,<sup>1</sup> Raphaële Clément,<sup>2</sup> Jihyun Jang,<sup>1,4,\*</sup> and Ying Shirley Meng<sup>1,5,6,\*</sup>

### SUMMARY

**Solid-state batteries are an emerging energy storage technology with the potential to offer improved safety, higher energy density, and longer cycle life. The solid electrolyte is a key component that determines the electrochemical performance of the solid-state battery, especially at room temperature. Herein, we report a series of nanocrystalline and amorphous chloride solid electrolytes with composition  $\text{Na}_{2.25-x}\text{Y}_{0.25}\text{Zr}_{0.75}\text{Cl}_{6-x}$  ( $1.375 \leq x \leq 2.000$ ) possessing enhanced ionic conductivity. This study employs X-ray diffraction, transmission electron microscopy, solid-state nuclear magnetic resonance spectroscopy, and electrochemical impedance spectroscopy to study the relationship between composition, structure, and conductivity. These results indicate that NaCl-deficient compositions can form both nanocrystalline and amorphous phases. Moreover, preferred occupancy of prismatic  $\text{Na}^+$  local environments and fast exchange between such environments were also observed. These factors together contribute to a low activation energy for  $\text{Na}^+$  hopping, increased ionic conductivity, and improved electrochemical performance at higher cycling rates while operating at room temperature.**

### INTRODUCTION

As society trends toward renewable energy sources, there is an undisputable need to implement energy storage devices that can both electrify transportation and complement intermittent power sources, like wind and solar. All-solid-state batteries (ASSBs) have recently emerged as a promising pathway forward as they can address the anticipated gap in energy storage capacity by theoretically providing much larger energy densities. When considering grid-level energy storage, a sustainable supply of ASSB materials must also be realized, and a low cost per kilowatt-hour is critical. As such, sodium ASSBs are advantageous for these large-scale applications, owing to the usage of intrinsically cheap and more abundant raw materials.<sup>1–3</sup> Moreover, sodium ASSBs have been shown to deliver stable long-term cycling, possibly enabling both a long battery lifetime and lower overall cost.<sup>4</sup>

Solid electrolytes (SEs) are the foundation of ASSBs, and as such play a primary role in the device's electrochemical performance. Inorganic SEs are a group of materials that can exhibit superionic conductivities at ambient temperature in both lithium- and sodium-based systems, some of which possess conductivities comparable to

### PROGRESS AND POTENTIAL

As the impacts of climate change are increasingly evident, society is acting by implementing renewable energy sources like wind and solar power. There is a need for safe and cost-effective energy storage devices to complement these intermittent power sources. Sodium solid-state batteries, which make use of more accessible and lower cost materials, are an emerging technology that potentially offer lower costs while operating safely. Although many  $\text{Li}^+$  chloride-based conductors have been explored, fewer  $\text{Na}^+$  analogs have been studied. As a result, their development lags with current materials possessing appreciably lower ionic conductivities that severely hinder battery kinetics. By significantly reducing the molar amount of NaCl to a fixed ratio of Y/Zr, we show that nanocrystalline and amorphous Na-Y-Zr-Cl phases with high conductivity can be synthesized. We believe this approach can be applied to other chlorides, which could lead to the discovery of other superionic conductors.

or even surpassing those of liquid-organic electrolytes.<sup>5</sup> Previously, ceramic and glass-ceramic materials, like NASICON-type oxide phases,  $\text{Na}_3\text{PS}_4$  (NPS), and  $\text{Na}_{2.88}\text{Sb}_{0.86}\text{W}_{0.11}\text{S}_4$  sulfides, have been found to exhibit some of the highest  $\text{Na}^+$  conductivities.<sup>6–10</sup> However, due to the high interfacial resistance between oxide SEs and cathode particles, additional high-temperature sintering steps are needed to achieve adequate interfacial contact and to reduce contact resistance.<sup>11</sup> Consequently, sulfide SEs have attracted a lot of attention due to their high ionic conductivities, while also exhibiting lower bulk moduli and thus better deformability under applied pressure at room temperature.<sup>12</sup> This favorable deformability leads to lower porosity and creates more surface contact area between the active materials and the SE.

Despite better processability, sulfide SEs suffer from a narrow electrochemical stability windows, which can lead to severe interfacial degradation reactions during cycling, yielding high interfacial resistance and inducing eventual cell failure.<sup>13</sup> While protective coatings have been applied to cathode particles to prevent side reactions between the cathode and SEs, the oxidation of sulfide SEs still occurs at high voltage and results in poor electrochemical performance.<sup>14,15</sup> Recently, it was shown that a bilayer electrolyte cell design utilizing NPS as the separator layer and a chloride-based catholyte in the cathode composite can avoid interfacial side reactions between NPS and the active material, thus delivering stable long-term cycling.<sup>4</sup> Therefore, developing a highly conductive SE or catholyte material that is stable over a wide range of potentials is essential for ASSB development. Such a material can enable the use of high-voltage cathode materials and improve long-term cyclability without the need for protective coating layers.

Within the past 5 years, chloride SEs have emerged as promising catholytes, offering excellent electrochemical stability at high voltages, high ionic conductivity, and good cyclability when paired with suitable oxide cathode materials.<sup>4,16–21</sup> In 2018, Asano et al. first reported the mechanochemical synthesis of  $\text{Li}_3\text{YCl}_6$  (LYC), which exhibited a high ionic conductivity of  $\sim 0.5 \text{ mS cm}^{-1}$ .<sup>16</sup> Interestingly, it was shown that the ionic conductivity of LYC decreased as the crystallinity of the phase increased. In the same work, it was proposed that, upon annealing,  $\text{Y}^{3+}$  cations in LYC occupy octahedral sites that are alternately stacked along the *c*-direction, which can partially block  $\text{Li}^+$  diffusion along that direction. Instead, low crystalline LYC possessing  $\text{Y}^{3+}$  anti-site defects was generated via mechanochemical ball milling, leading to reduced crystallinity and improved ionic conductivity.<sup>16</sup> Sebti et al. showed that, rather than random disorder on the Y lattice, Y layer stacking faults in LYC are formed during ball milling, opening up new  $\text{Li}^+$  transport pathways and drastically lowering  $\text{Li}^+$  diffusion barriers throughout the structure, thus increasing intragrain transport.<sup>22</sup>

Besides crystallinity, the concentration of vacancies also plays an important role in the resultant ionic conductivity. Aliovalent substitution strategies have been implemented to create additional vacancies that enhance ionic transport.<sup>4,23</sup> Recently, Liang et al. explored the composition variation between  $\text{LiCl}$  and  $\text{ScCl}_3$ , yielding a series of  $\text{Li}_x\text{ScCl}_{3+x}$  ( $1 \leq x \leq 4$ ) SEs. The authors showed that  $\text{Li}^+$  conductivity and activation energy vary significantly with the ratio of  $\text{LiCl}$  to  $\text{ScCl}_3$  used during synthesis, and they attributed the highest ionic conductivity to a balancing effect between the concentration of  $\text{Li}^+$  charge carriers and vacancies.<sup>24</sup> Although the precise structure of these  $\text{Li}_x\text{ScCl}_{3+x}$  phases remains unclear, the concept is promising as it can enhance the materials' ionic conductivity without the incorporation of additional transition metals.

<sup>1</sup>Department of NanoEngineering, University of California, San Diego, La Jolla, CA 92093, USA

<sup>2</sup>Department of Materials, University of California, Santa Barbara, Santa Barbara, CA 93117, USA

<sup>3</sup>Materials Science and Engineering Program, University of California, San Diego, La Jolla, CA 92093, USA

<sup>4</sup>Department of Chemistry, Sogang University, Mapo-gu, Seoul 04107, Republic of Korea

<sup>5</sup>Pritzker School of Molecular Engineering, The University of Chicago, Chicago, IL 60637, USA

<sup>6</sup>Lead contact

\*Correspondence:  
[jihyunjang@sogang.ac.kr](mailto:jihyunjang@sogang.ac.kr) (J.J.),  
[shirlymeng@uchicago.edu](mailto:shirlymeng@uchicago.edu) (Y.S.M.)

<https://doi.org/10.1016/j.matt.2023.12.028>

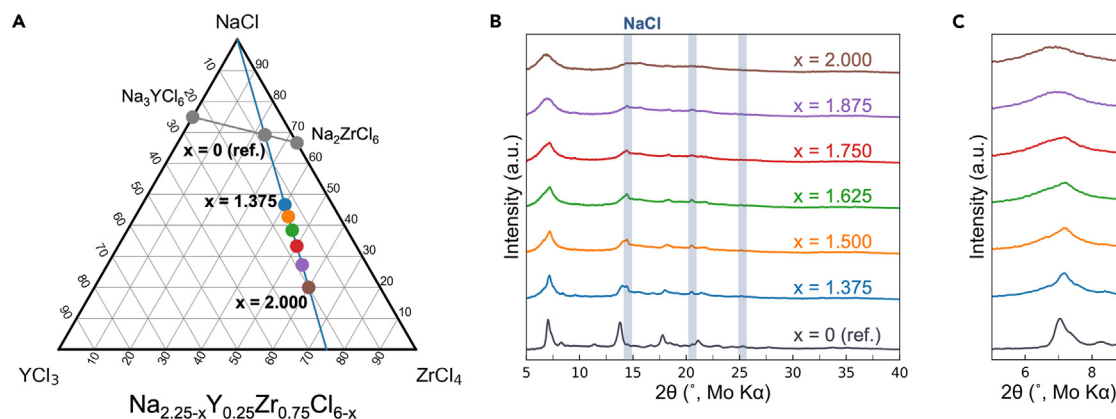


**Figure 1. Na-Y-Zr-Cl composition and long-range order**

(A) Ternary composition diagram of NaCl, YCl<sub>3</sub>, and ZrCl<sub>4</sub> precursor compounds demonstrating the molar ratios explored in this work. (B) XRD patterns of Na<sub>2.25-x</sub>Y<sub>0.25</sub>Zr<sub>0.75</sub>Cl<sub>6-x</sub> (1.375 ≤ x ≤ 2) SEs. (C) Expanded XRD patterns of Na<sub>2.25-x</sub>Y<sub>0.25</sub>Zr<sub>0.75</sub>Cl<sub>6-x</sub> (1.375 ≤ x ≤ 2) SEs, highlighting the main diffraction peaks in the 5–9 2θ range.

Sodium chloride-based analog materials, derived from Na<sub>3</sub>MCl<sub>6</sub> and Na<sub>2</sub>MCl<sub>6</sub> compounds (M<sup>3+</sup> = Y<sup>3+</sup>, Er<sup>3+</sup>, Gd<sup>3+</sup>, and M<sup>4+</sup> = Zr<sup>4+</sup>), have also emerged as promising catholytes for Na-ASSBs.<sup>25–28</sup> Mechanochemical syntheses of Na<sub>3</sub>YCl<sub>6</sub>, Na<sub>3</sub>ErCl<sub>6</sub>, and Na<sub>2</sub>ZrCl<sub>6</sub> have all yielded relatively low Na<sup>+</sup> conductivities (≤10<sup>-5</sup> S cm<sup>-1</sup>) and have thus required the implementation of aliovalent substitution. Consequently, the synthesis of Na<sub>3-y</sub>Y<sub>1-y</sub>Zr<sub>y</sub>Cl<sub>6</sub> (0 ≤ y ≤ 1) solid solutions was recently reported, with the maximum ionic conductivity observed for the y = 0.75 composition.<sup>4</sup> This increased ionic conductivity was attributed to the introduction of Na<sup>+</sup> vacancies, an optimal unit cell volume, and cooperative MCl<sub>6</sub> rotations.<sup>4,29,30</sup> Moreover, it was observed that the ionic conductivity of the y = 0.75 composition was lower after crystallization from heat treatment and reached its highest value after mechanochemical milling. As ball milling is known to reduce grain sizes and introduce defects, these results indicate a strong relationship between crystallinity and ionic conductivity as has generally been observed for chloride-based SEs. Therefore, the design of Na-chloride SEs should be focused on optimizing crystallinity and the concentration of Na<sup>+</sup> vacancies to promote more favorable Na<sup>+</sup> diffusion.

In this study, we investigate the synergistic effects of sample crystallinity and NaCl content on the ionic conductivity of Na<sub>3-y</sub>Y<sub>1-y</sub>Zr<sub>y</sub>Cl<sub>6</sub> SEs. To minimize the total number of variables, the Y/Zr ratio was fixed at 1/3, corresponding to the highest ionic conductivity previously observed across the Na<sub>3-y</sub>Y<sub>1-y</sub>Zr<sub>y</sub>Cl<sub>6</sub> series. Thus, only the NaCl molar content was varied, leading to the Na<sub>2.25-x</sub>Y<sub>0.25</sub>Zr<sub>0.75</sub>Cl<sub>6-x</sub> (1.375 ≤ x ≤ 2.000) compositional series. Our findings show that by tuning the composition, and in particular by forming NaCl-deficient compounds, nanocrystalline and amorphous SEs with high Na<sup>+</sup> conductivities can be obtained. The enhanced ionic conductivity is attributed to the synergistic effects of reduced grain size, the preferred occupancy of rapidly exchanging prismatic Na<sup>+</sup> local environments, and an increased number of Na<sup>+</sup> vacancies in the NaCl-poor compounds, all of which serve to improve the performance of ASSBs, especially at high cycling rates and while operating at room temperature.

## RESULTS AND DISCUSSION

### Sample crystallinity and microstructure

Figure 1A displays the ternary composition diagram of NaCl, YCl<sub>3</sub>, and ZrCl<sub>4</sub>, where the points in blue illustrate the molar ratios explored in this work, e.g., Na<sub>2.25-x</sub>Y<sub>0.25</sub>Zr<sub>0.75</sub>Cl<sub>6-x</sub>

( $1.325 \leq x \leq 2.000$ ). For reference, the previously reported ternary phases  $\text{Na}_3\text{YCl}_6$  and  $\text{Na}_2\text{ZrCl}_6$ , and the aliovalently substituted  $\text{Na}_{2.25}\text{Y}_{0.25}\text{Zr}_{0.75}\text{Cl}_6$  ( $x = 0$ ) phase, are shown in orange.<sup>4</sup> X-ray diffraction (XRD) patterns obtained on the  $\text{Na}_{2.25-x}\text{Y}_{0.25}\text{Zr}_{0.75}\text{Cl}_{6-x}$  samples after ball milling exhibit only several low-intensity diffraction peaks (Figure 1B). Notably, no significant diffraction peaks from the  $\text{NaCl}$ ,  $\text{YCl}_3$ , or  $\text{ZrCl}_4$  precursors are observed after ball milling, except from a small amount of  $\text{NaCl}$  impurity in the high-sodium-containing samples (when  $x \leq 1.875$ ). The observable diffraction peaks for the  $\text{Na}_{2.25}\text{Y}_{0.25}\text{Zr}_{0.75}\text{Cl}_6$  compositional series are remarkably broad, indicating the formation of low crystallinity products. This is likely due to small crystallite sizes and strain broadening effects arising from particle fracturing and the introduction of defects during the harsh mechanochemical synthesis step.<sup>31–34</sup> Interestingly, as the  $\text{NaCl}$  molar content is reduced, or the  $x$  value in  $\text{Na}_{2.25-x}\text{Y}_{0.25}\text{Zr}_{0.75}\text{Cl}_{6-x}$  is increased from  $x = 1.375$  to  $x = 2.000$ , a general broadening of the main diffraction peaks at low  $2\theta$  angles is observed, as shown in Figure 1C, suggesting that  $\text{NaCl}$ -poor compositions tend to form smaller domain sizes. Interestingly, at the composition where the  $\text{NaCl}$  molar content is lowest ( $x = 2.000$ ), the diffraction pattern is nearly featureless, and the main reflection is noticeably broad, which indicates that the obtained phase lacks any significant long-range ordering.

To analyze the microstructure of the sample, transmission electron microscopy (TEM) and selected area electron diffraction (SAED) experiments were conducted on the end-member and intermediate compositions (i.e.,  $x = 1.375$ ,  $1.625$ , and  $2.000$ ). TEM images (Figures 2A–2C) show SE particles ranging from  $\sim 1$  to  $2 \mu\text{m}$  in size, similar to the scanning electron microscopy (SEM) images (Figure S1) collected on the same samples. SAED images for the  $x = 1.375$  and  $x = 1.625$  compositions (Figures 2D and 2E) reveal signatures of an  $\text{NaCl}$  impurity, as indicated by the diffraction rings in Figure 2D and diffraction spots in Figure 2E, which correspond to the  $d$ -spacing of the marked lattice planes (radially integrated intensities shown in Figure S2). The remaining powder rings with larger  $d$ -spacing can be attributed to the main XRD peaks at lower  $2\theta$  (Figure 1B) and correspond to the  $\text{Na}_{2.25}\text{Y}_{0.25}\text{Zr}_{0.75}\text{Cl}_6$  phase (marked in white as NYZC). Furthermore, the smoothness and absence of individual reflections in the NYZC diffraction rings for the  $x = 1.375$  and  $x = 1.625$  compositions indicate that these samples are not only polycrystalline but possess very fine or even nanocrystalline grains. Conversely, the diffraction rings of the  $x = 2.000$  sample merge, and a halo pattern (Figure 2F) is observed, suggesting that samples at higher  $x$  values only exhibit short-range order. However, the presence of an amorphous phase for compositions of  $x < 2.000$  cannot be entirely ruled out as some fractions of amorphous products are normally expected to be present in the sample when mechanochemical synthesis approaches are used. Although it can be difficult to discern between nanocrystalline and fully amorphous states when analyzing bulk XRD patterns, the complementary TEM and SAED analyses indicate that the samples transition from a nanocrystalline state to a fully amorphous state as  $x$  increases from  $1.375$  to  $2.000$  in  $\text{Na}_{2.25-x}\text{Y}_{0.25}\text{Zr}_{0.75}\text{Cl}_{6-x}$ .

### Local Na environment and ionic conductivity

Due to the nanocrystalline and amorphous nature of the  $\text{Na}_{2.25-x}\text{Y}_{0.25}\text{Zr}_{0.75}\text{Cl}_{6-x}$  ( $1.325 \leq x \leq 2.000$ ) compositional series, local Na environments in these different samples were studied using  $^{23}\text{Na}$  solid-state nuclear magnetic resonance (ss-NMR) spectroscopy. The resulting room temperature  $^{23}\text{Na}$  ss-NMR spectra are presented in Figure 3A. The peak located around  $7.2 \text{ ppm}$ , observed in almost all of the samples, is attributed to unreacted  $\text{NaCl}$  precursor,<sup>4,35</sup> which agrees well with the XRD and SAED results. The  $\text{NaCl}$  impurity was quantified and determined to be  $\sim 4 \text{ wt } \%$  on average (Table S2). As the molar content of  $\text{NaCl}$  decreases ( $x$  increases) in the

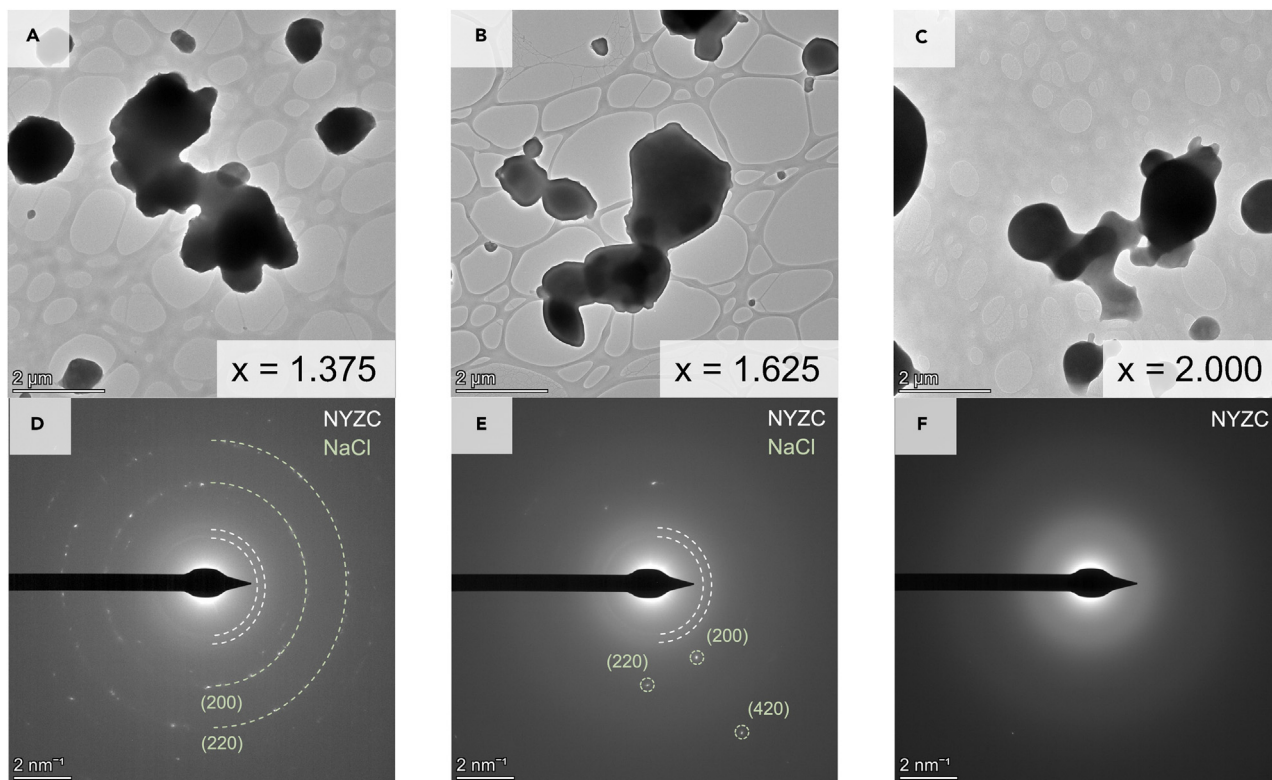


**Figure 2. Sample microstructure and crystallinity**

(A–C) TEM for  $\text{Na}_{2.25-x}\text{Y}_{0.25}\text{Zr}_{0.75}\text{Cl}_{6-x}$  materials ( $x = 1.375, 1.625,$  and  $2.000$ , respectively).

(D–F) Selected area electron diffractions for  $\text{Na}_{2.25-x}\text{Y}_{0.25}\text{Zr}_{0.75}\text{Cl}_{6-x}$  materials ( $x = 1.375, x = 0.1625,$  and  $x = 2.000$ , respectively).

sample, a corresponding reduction in NaCl signal intensity is observed. To obtain the specific composition of the  $\text{Na}_{2.25-x}\text{Y}_{0.25}\text{Zr}_{0.75}\text{Cl}_{6-x}$  ( $1.325 \leq x \leq 2.000$ ) samples, adjusted  $x$  values were calculated by comparing ss-NMR signal areas from the resonances attributed to NaCl and  $\text{Na}_{2.25-x}\text{Y}_{0.25}\text{Zr}_{0.75}\text{Cl}_{6-x}$  phases (Figure S4). Our analysis shows that these adjusted  $x$  values are slightly higher but generally vary linearly with the stoichiometric  $x$  value, showing that higher  $x$  values clearly result in decreasing NaCl contents. Furthermore, the two weak and broad signals detected in the range of about  $-2.5$  to  $8$  ppm are attributed to octahedral Na environments, while the intense resonance between about  $-10$  and  $-13$  ppm is assigned the Na in (a) prismatic environment(s) on the basis of the  $^{23}\text{Na}$  ss-NMR data and first-principles calculations of NMR shifts previously reported for the related, crystalline  $\text{Na}_{2.25}\text{Y}_{0.25}\text{Zr}_{0.75}\text{Cl}_6$  compound.<sup>30</sup> Interestingly, the prismatic Na resonance can clearly be observed at all values of  $x$ , while signals corresponding to octahedral Na environments can only be detected when  $x \leq 1.750$ . Hence,  $\text{Na}^+$  ions tend to first occupy prismatic environments, which is similar to what has been reported in some chloride SEs.<sup>23,30</sup> With more Na in octahedral sites in the samples at higher NaCl contents, the prismatic resonance shifts toward more positive ppm frequencies (toward the octahedral Na resonances) and broadens. This evolution could be attributed to changes in Na mobility and increased chemical exchange between prismatic and octahedral sites, resulting in a broadening of the corresponding  $^{23}\text{Na}$  NMR resonances that draw closer to one another in the intermediate exchange regime, i.e., when the exchange constant ( $k_{\text{ex}}$ ) is on par with the frequency separation of the resonances corresponding to the exchanging sites ( $\Delta\nu$ , in Hz).<sup>36</sup> Two-dimensional  $^{23}\text{Na}$

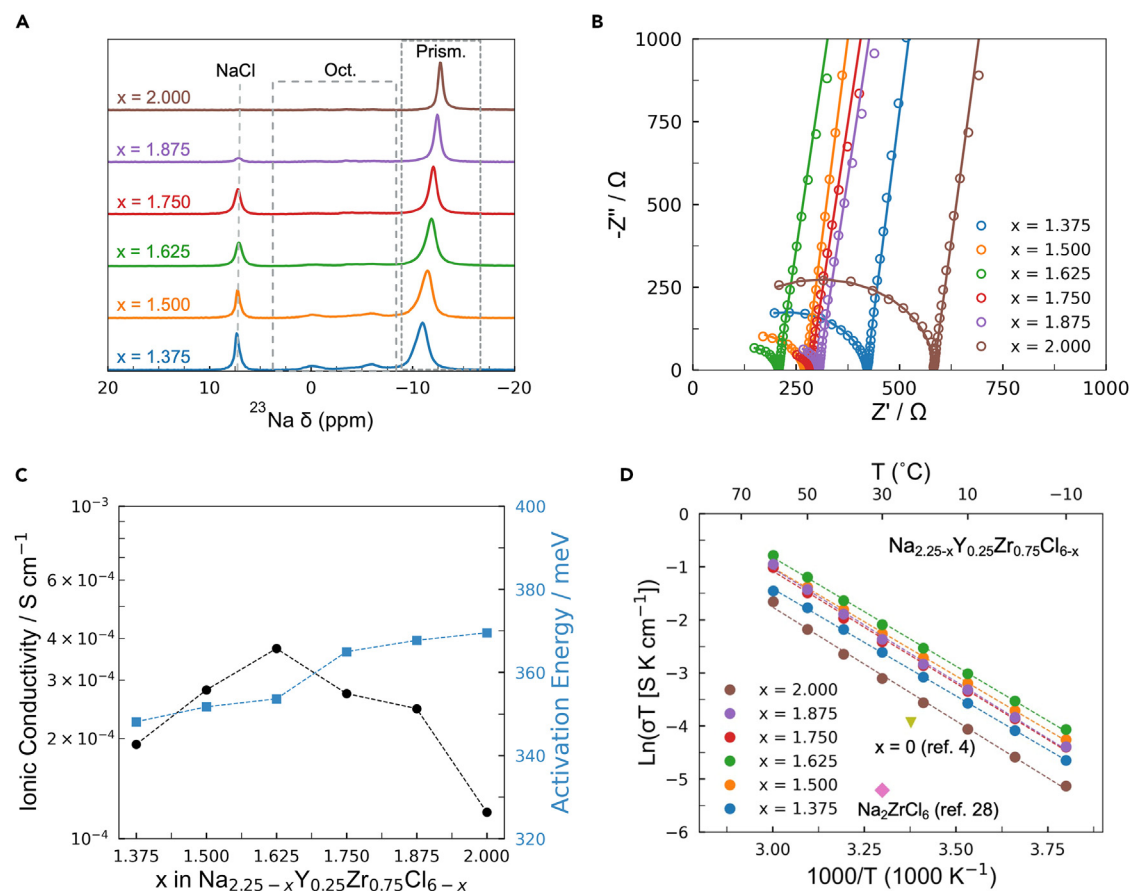


**Figure 3. Sodium local environments and ionic conductivity measurements**

(A) Room temperature  $^{23}\text{Na}$  ss-NMR spectra collected on the various  $\text{Na}_{2.25-x}\text{Y}_{0.25}\text{Zr}_{0.75}\text{Cl}_{6-x}$  ( $1.375 \leq x \leq 2$ ) compositions at 18.8 T and at a magic angle spinning frequency of 12 kHz.

(B) Room temperature ionic conductivity measurements with fits (equivalent circuit model shown in Figure S6) for the various  $\text{Na}_{2.25-x}\text{Y}_{0.25}\text{Zr}_{0.75}\text{Cl}_{6-x}$  ( $1.375 \leq x \leq 2$ ) compositions.

(C) Comparison of room temperature ionic conductivities and activation energies for the various  $\text{Na}_{2.25-x}\text{Y}_{0.25}\text{Zr}_{0.75}\text{Cl}_{6-x}$  ( $1.375 \leq x \leq 2$ ) compositions.

(D) Arrhenius conductivity plots for the various  $\text{Na}_{2.25-x}\text{Y}_{0.25}\text{Zr}_{0.75}\text{Cl}_{6-x}$  ( $1.375 \leq x \leq 2$ ) compositions.

exchange spectroscopy experiments, carried out on the  $x = 1.625$  composition, show that Na in octahedral and prismatic sites have the possibility to be in exchange (Figure S5). Nevertheless, a structural explanation cannot be ruled out as the impact on  $^{23}\text{Na}$  chemical shift from possible structural differences such as lattice constant variation and increased Na site disorder is unknown.

Figure 3B shows the room temperature Nyquist plots obtained from electrochemical impedance spectroscopic (EIS) measurements on all of the  $\text{Na}_{2.25-x}\text{Y}_{0.25}\text{Zr}_{0.75}\text{Cl}_{6-x}$  compositions, while the evolution of the ionic conductivity with  $x$  is presented in Figure 3C. All SE samples exhibit high  $\text{Na}^+$  conductivities ( $>1.0 \times 10^{-4} \text{ S cm}^{-1}$ ), with a maximum value of  $4.0 \times 10^{-4} \text{ S cm}^{-1}$  for the  $x = 1.625$  composition. Notably, these conductivity values are all significantly higher than what has previously been reported for Na-Y-Zr-Cl phases.<sup>4</sup> Moreover, DC polarization measurements (Figure S7) confirm that electronic conduction is negligible, with all compositions exhibiting electronic conductivities on the order of  $10^{-9} \text{ S cm}^{-1}$ , as summarized in Table S1. As the NaCl content is decreased below  $x = 1.625$ , the ionic conductivity begins to drop. Yet the sample with the lowest molar content of NaCl ( $x = 2.000$ ) still exhibits an ionic conductivity of

$1.2 \times 10^{-4} \text{ S cm}^{-1}$ , which is comparable to cubic NPS ( $1.4 \times 10^{-4} \text{ S cm}^{-1}$ ) and is still higher than all other previously reported chloride-based Na-ion conductors.<sup>4,23,28,37</sup> The high conductivity of  $\text{Na}_{2.25-x}\text{Y}_{0.25}\text{Zr}_{0.75}\text{Cl}_{6-x}$  compounds at high  $x$  is likely in part due to a vacancy-mediated  $\text{Na}^+$  transport mechanism and a high Na mobility afforded by the high concentration of Na vacancies per unit volume.

Arrhenius plots obtained for all  $\text{Na}_{2.25-x}\text{Y}_{0.25}\text{Zr}_{0.75}\text{Cl}_{6-x}$  compositions show that  $\ln(\sigma T)$  vs.  $1/T$  evolves linearly within the temperature range probed (Figure 3D). Thus, the activation energy for  $\text{Na}^+$  diffusion can be extracted by linearizing the Arrhenius equation:

$$\sigma = \frac{\sigma_0}{T} e^{-\frac{E_a}{k_B T}}, \quad (\text{Equation 1})$$

where  $\sigma_0$  is the Arrhenius pre-factor,  $E_a$  is the activation energy, and  $k_B$  is the Boltzmann constant.

All  $\text{Na}_{2.25-x}\text{Y}_{0.25}\text{Zr}_{0.75}\text{Cl}_{6-x}$  compositions possess activation energies in the range of 348–370 meV (Table S1, corresponding to the Nyquist plots shown in Figure S9), which are all appreciably lower than that of the reference  $\text{Na}_{2.25}\text{Y}_{0.25}\text{Zr}_{0.75}\text{Cl}_6$  phase (664 meV) and again fairly similar to cubic NPS (364 meV).<sup>4,37</sup> The evolution of the activation energy and ionic conductivity with NaCl content  $x$  is shown in Figure 3D, and it demonstrates that there is little to no correlation between the measured ionic conductivity and the activation energy, as has been reported for other amorphous ionic conductors.<sup>38</sup>

Because amorphous materials possess lower densities than their crystalline counterparts, free volume—a consequence of their non-periodicity and lower packing densities—is allowed.<sup>39</sup> Free volume has been previously shown to facilitate ion mobility and thus enhance ionic conductivity.<sup>40,41</sup> Here, it is speculated that the nanocrystalline and amorphous nature of the  $\text{Na}_{2.25-x}\text{Y}_{0.25}\text{Zr}_{0.75}\text{Cl}_{6-x}$  compounds leads to more free volume compared to the more crystalline reference  $\text{Na}_{2.25}\text{Y}_{0.25}\text{Zr}_{0.75}\text{Cl}_6$  SE, which may be one contributing factor to the improved  $\text{Na}^+$  mobility and lower migration energy barriers. Additionally, as the ratio of Y/Zr is fixed, a reduction in NaCl content will also reduce the population of  $\text{Na}^+$  sites, leading to an increased concentration of Na vacancies that could further aid  $\text{Na}^+$  transport. However, since the total conductivity is a product of  $n_{\text{Na}}$  and  $\mu_{\text{Na}}$ , a balance must be struck between the two to achieve the highest conductivity, as the ionic conductivity of a single ion conductor is determined by the following relation:

$$\sigma = n_i q_i \mu_i, \quad (\text{Equation 2})$$

where  $\sigma$  is the ionic conductivity,  $n_i$  is the number of charge carriers of species  $i$ ,  $q_i$  is the charge of species  $i$ , and  $\mu_i$  is the mobility of species  $i$ .

Although <sup>23</sup>Na ss-NMR suggests that  $\text{Na}^+$  mobility increases at higher  $x$  values, there will be an insufficient number of charge carriers when the concentration of  $\text{Na}^+$  per unit volume is too low. As such, the  $\text{Na}_{0.625}\text{Y}_{0.25}\text{Zr}_{0.75}\text{Cl}_{4.375}$  ( $x = 1.625$ ) composition appears to be the optimal composition, balancing the concentration of mobile  $\text{Na}^+$  charge carriers and their mobility.

### Crystallization behavior of $\text{Na}_{2.25-x}\text{Y}_{0.25}\text{Zr}_{0.75}\text{Cl}_{6-x}$ solid electrolytes

To better understand the impact of sample crystallinity and local structure on  $\text{Na}^+$  mobility, the composition with the highest ionic conductivity ( $x = 1.625$ ) and the fully amorphous ( $x = 2.000$ ) sample were selected for further study. These two samples



were heat treated at 100°C for 2 h to induce crystallization. This temperature was selected based on differential scanning calorimetry measurements (Figure S8), where an exothermic phase transition (i.e., crystallization) was observed to have an onset temperature below 100°C.

XRD patterns of the two compositions ( $x = 1.625$  and  $x = 2.000$ ) were collected after the thermal treatment step and are shown in Figure 3A. In the case of the  $x = 1.625$  composition, upon heating, all linewidths of the diffraction peaks associated with the  $\text{Na}_{2.25-x}\text{Y}_{0.25}\text{Zr}_{0.75}\text{Cl}_{6-x}$  phase become significantly narrower, which is attributed to crystallization. For the  $x = 2.000$  composition, new diffraction peaks corresponding to the  $\text{Na}_{2.25-x}\text{Y}_{0.25}\text{Zr}_{0.75}\text{Cl}_{6-x}$  phase appear along with the highest intensity diffraction peak for crystalline  $\text{ZrCl}_4$  corresponding to the (121) plane. However, the broad diffraction peak at low  $2\theta$  angles, corresponding to the amorphous constituent, is still apparent after heat treatment, suggesting incomplete crystallization.

A comparison of the  $^{23}\text{Na}$  ss-NMR spectra obtained on the  $x = 1.625$  sample before and after the heat treatment shows that the excess NaCl in the pristine (untreated) sample is consumed and incorporated into the  $\text{Na}_{2.25-x}\text{Y}_{0.25}\text{Zr}_{0.75}\text{Cl}_{6-x}$  phase when the sample is subjected to heating at 100°C (Figure 4B). Furthermore, the signal corresponding to prismatic Na broadens and decreases in intensity, while the signals attributed to octahedral Na environments grow significantly. A similar evolution of the  $^{23}\text{Na}$  NMR spectrum is observed for the  $x = 2.000$  sample. Thus, the 100°C heat treatment promotes crystallization of these two  $\text{Na}_{2.25-x}\text{Y}_{0.25}\text{Zr}_{0.75}\text{Cl}_{6-x}$  phases, which is accompanied by a redistribution of Na from prismatic environments to octahedral sites in the structure and increased exchange between the environments. Consequently, the two crystallized samples exhibit roughly one order of magnitude lower ionic conductivities and increased activation energies compared to their nanocrystalline/amorphous analogs (Figures 4C and 4D, Nyquist plots shown in Figures S6 and S10). This finding agrees well with the decrease in conductivity observed for some disordered chloride SEs subjected to a heat treatment or annealing step.<sup>4,16,28</sup> Clearly, for the  $\text{Na}_{2.25-x}\text{Y}_{0.25}\text{Zr}_{0.75}\text{Cl}_{6-x}$  compounds of interest to the present work, smaller grain sizes and amorphization lead to rapid  $\text{Na}^+$  exchange between prismatic sites, which are key for achieving high  $\text{Na}^+$  conductivity.

### Electrochemical testing

The room temperature performance of two solid-state batteries comprising either the most conductive  $\text{Na}_{2.25-x}\text{Y}_{0.25}\text{Zr}_{0.75}\text{Cl}_{6-x}$  compound ( $x = 1.625$ ) or the fully amorphous compound ( $x = 2.000$ ) was evaluated. Before assembling the solid-state batteries, the electrochemical stability window of the two materials was examined using linear sweep voltammetry (Figure 5A). The  $x = 1.625$  and  $x = 2.000$  samples exhibit a peak oxidation current at  $\sim 4.6$  and  $4.7$  V vs. the reference electrode ( $\text{Na}_9\text{Sn}_4$ ), with the onset of this peak taking place near  $4.0$  and  $4.1$  V, respectively. During the reduction sweep, both samples show two reduction peaks at  $\sim 1.4$  and  $0.55$  V vs. the reference, which can be attributed to  $\text{Zr}^{4+}$  and  $\text{Y}^{3+}$  reduction, respectively,<sup>4,42</sup> with the onset of the first reduction peak occurring around  $1.8$  to  $2.0$  V vs. the reference electrode. Consequently, both samples exhibit a wide electrochemical window and are thus compatible with various sodium-based cathode materials (Figure 5B), making them ideal catholyte materials.  $\text{NaCrO}_2$  was selected to be paired with both  $\text{Na}_{2.25-x}\text{Y}_{0.25}\text{Zr}_{0.75}\text{Cl}_{6-x}$  compositions due to its suitable voltage window ( $1.7$ – $3.4$  V), relatively high specific capacity ( $120 \text{ mAh g}^{-1}$ ), and excellent reversibility.

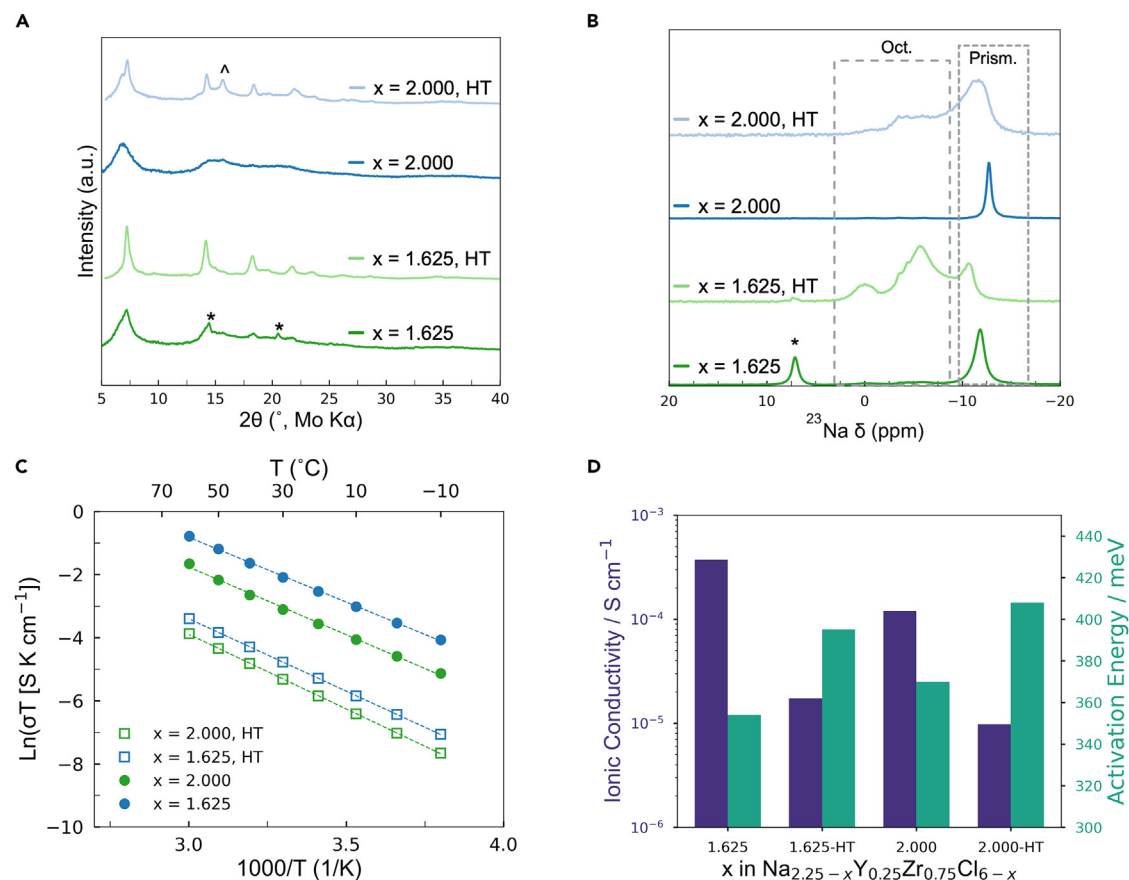


**Figure 4. Effect of solid electrolyte crystallinity on ionic conductivity**

(A) X-ray diffraction patterns for the ball-milled and heat-treated  $x = 1.625$  and  $x = 2.000$  compositions. Asterisk (\*) indicates XRD peaks attributed to NaCl, and circumflex (^) indicates XRD peak ascribed to ZrCl<sub>4</sub>.

(B) Room temperature <sup>23</sup>Na ss-NMR spectra for the  $x = 1.625$  and  $x = 2.000$  compositions at 18.8 T and at a magic angle spinning frequency of 12 kHz. The asterisk (\*) indicates the NaCl resonance.

(C) Arrhenius conductivity plots for the ball-milled and heat-treated  $x = 1.625$  and  $x = 2.000$  compositions.

(D) Comparison bar plots of room temperature ionic conductivity and activation energy for the ball-milled and heat-treated  $x = 1.625$  and  $x = 2.000$  compositions.

All-solid-state cells using the  $x = 1.625$  and  $x = 2.000$  catholytes were assembled and cycled at room temperature using an areal loading of 1 mAh cm<sup>-2</sup> (Figure 4A). At a 0.1 C current rate (where 1 C = 120 mA g<sup>-1</sup> or 100  $\mu$ A cm<sup>-2</sup>), both compositions deliver high initial charge and discharge capacities (Figure 6A), with initial Coulombic efficiency (ICE) values of >96%. These high ICE values are attributed to the good electrochemical compatibility between the catholyte and the NaCrO<sub>2</sub> cathode. Both compounds are able to deliver near theoretical capacity for NaCrO<sub>2</sub> ( $\sim$ 126 mAh g<sup>-1</sup>), presumably due to their high ionic conductivities. Moreover, the deformability of these Na<sub>2.25-x</sub>Y<sub>0.25</sub>Zr<sub>0.75</sub>Cl<sub>6-x</sub> catholytes is advantageous as it leads to good contact between cathode and SE particles under cold-pressing conditions, a more uniform current density distribution, and better utilization of the cathode active material in the composite (Figure S11).<sup>43</sup> This can be evidenced by two-dimensional porosity values, which were calculated for a heat-treated  $x = 0$  (4.9%) and an as-milled  $x = 1.625$  (0.2%) phase, whereby cross-sectional focused ion beam-SEM images were binarized, and black pixels were assigned to void space (Figure S12). Besides the softer nature of the chloride anion framework compared to oxide SEs, we hypothesize that the nanocrystalline and amorphous nature of the

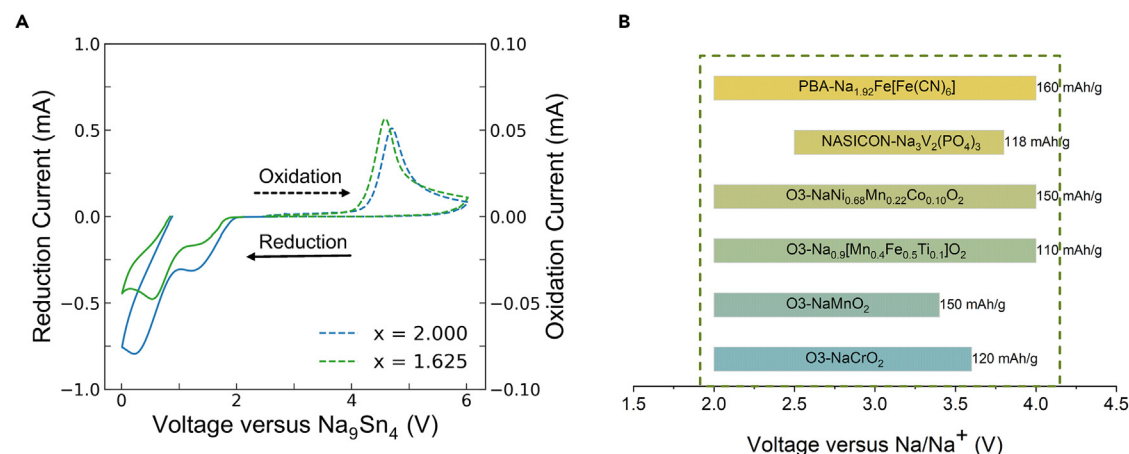


**Figure 5. Electrochemical stability window of catholytes**

(A) Oxidation and reduction linear sweep voltammetry curves for  $x = 1.625$  and  $x = 2.000$  samples of the  $\text{Na}_{2.25-x}\text{Y}_{0.25}\text{Zr}_{0.75}\text{Cl}_{6-x}$  composition series. Note the difference in scaling for the left-hand and right-hand x axis.

(B) Comparison of electrochemical active windows for various sodium-based cathode materials.

present samples could further contribute to their good experimentally observed deformability.

Rate capability tests using a sequence of 0.1, 0.2, 0.5, 1.0, and 0.1 C current rates also revealed that both solid-state cells exhibit excellent performance at higher current densities (Figures 6B and 6C). The performance of the two cells shows little difference at lower C-rates (0.1 and 0.2 C) or even at higher C-rates (0.5 and 1 C), which is likely due to the similar ionic conductivity values of the  $x = 1.625$  and  $x = 2.000$  catholytes. Interestingly, at higher current rates, both compositions show good utilization of the cathode active material, reversibly delivering  $\sim 105 \text{ mAh g}^{-1}$  and  $\sim 97 \text{ mAh g}^{-1}$  of capacity at 0.5 and 1 C, respectively.

Beyond the rate study, extended cycling at 0.33 C shows that the two cells containing the  $x = 1.625$  and  $x = 2.000$  catholytes demonstrate reversible and stable cycling (Figures 6D and 6E). Average Coulombic efficiencies (CEs) of 99.95% and 99.96%, and capacity retentions of 78% and 83%, are obtained after 500 cycles for the  $x = 1.625$  and  $x = 2.000$  cells, respectively. The high CEs and low capacity fading at room temperature can be credited to the catholyte being electrochemically stable within the cycling conditions. Previously, the oxidative stability window for the stoichiometric  $\text{Na}_{2.25}\text{Y}_{0.25}\text{Zr}_{0.75}\text{Cl}_6$  ( $x = 0$ ) catholyte was reported to be upward of 3.8 V vs.  $\text{Na}/\text{Na}^+$ .<sup>4</sup> Here, a similar electrochemical stability window is observed for both the  $x = 1.625$  and  $x = 2.000$  compositions. The electrochemical tests conducted here highlight the benefits of utilizing a chloride-based catholyte with high ionic conductivity and oxidative stability, resulting in good room-temperature cell performance.

## Conclusions

This study presents an alternative approach for developing highly conductive  $\text{Na}^+$  conductors with nanocrystalline and/or amorphous characteristics. This method involves adjusting the NaCl composition to a fixed ratio of Y/Zr in  $\text{Na}_{2.25-x}\text{Y}_{0.25}\text{Zr}_{0.75}\text{Cl}_{6-x}$  compounds while utilizing mechanochemical synthesis to control the long-range and local structure. The as-milled samples obtained from this approach exhibit preferential occupation of prismatic sites by Na and fast Na chemical exchange between those sites. Moreover, the reduced NaCl content, when combined

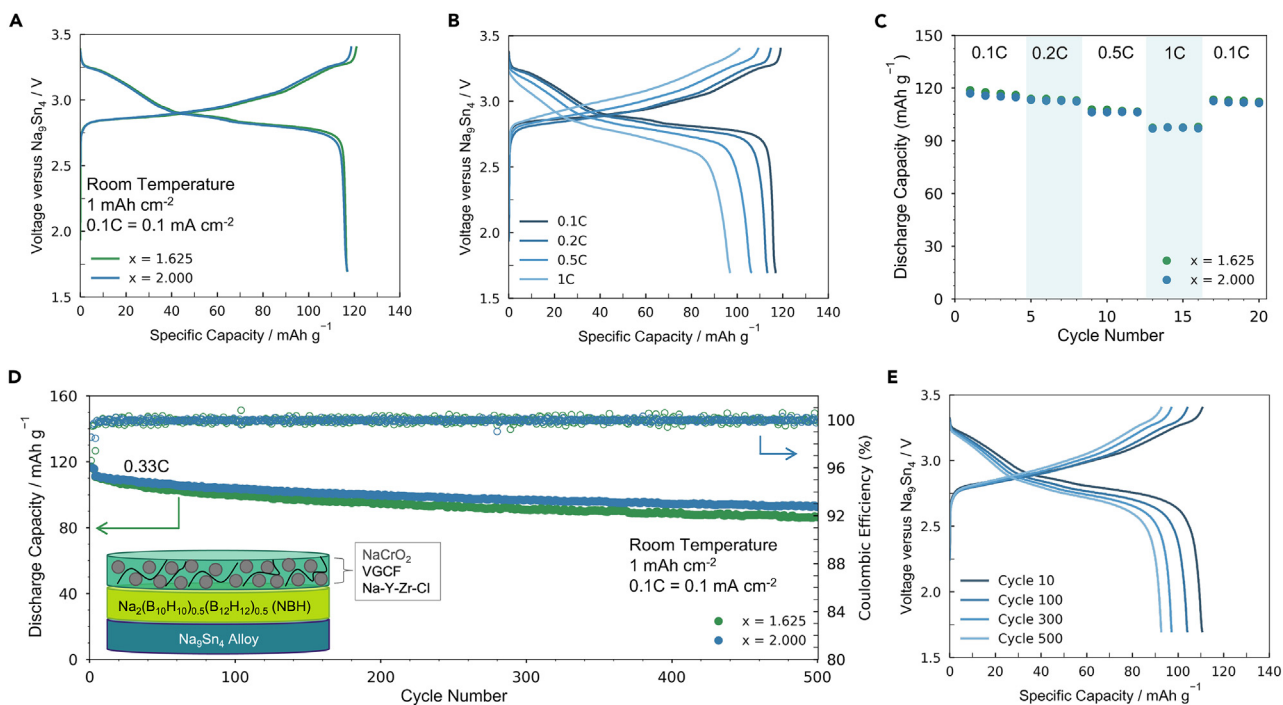


**Figure 6. Electrochemical performance of nanocrystalline and amorphous SEs**

(A) First cycle voltage profile of  $\text{Na}_{0.625}\text{Y}_{0.25}\text{Zr}_{0.75}\text{Cl}_{4.375}$  ( $x = 1.625$ ) and  $\text{Na}_{0.25}\text{Y}_{0.25}\text{Zr}_{0.75}\text{Cl}_4$  ( $x = 2.000$ ) catholytes paired with a  $\text{NaCrO}_2$  cathode.  
 (B) Voltage profiles at varying C-rates for  $\text{Na}_{0.25}\text{Y}_{0.25}\text{Zr}_{0.75}\text{Cl}_4$  ( $x = 2.000$ ) material.  
 (C) Rate study comparison for  $\text{Na}_{0.625}\text{Y}_{0.25}\text{Zr}_{0.75}\text{Cl}_{4.375}$  ( $x = 1.625$ ) and  $\text{Na}_{0.25}\text{Y}_{0.25}\text{Zr}_{0.75}\text{Cl}_4$  ( $x = 2.000$ ) materials.  
 (D) Extended cell cycling at 0.33C rate for  $\text{Na}_{0.625}\text{Y}_{0.25}\text{Zr}_{0.75}\text{Cl}_{4.375}$  ( $x = 1.625$ ) and  $\text{Na}_{0.25}\text{Y}_{0.25}\text{Zr}_{0.75}\text{Cl}_4$  ( $x = 2.000$ ) materials.  
 (E) Voltage profiles corresponding to the extending cycling data for  $\text{Na}_{0.25}\text{Y}_{0.25}\text{Zr}_{0.75}\text{Cl}_4$  ( $x = 2.000$ ) solid electrolyte.

with mechanochemical synthesis, results in the formation of samples that are either nanocrystalline or amorphous. This introduces defects and free volume into the system, which presumably contribute to the enhanced  $\text{Na}^+$  mobility. Such factors were evidenced using a wide range of bulk and localized characterization techniques like XRD, TEM, SAED, ss-NMR, and EIS measurements. The increased ionic conductivity of compositions with a low NaCl content leads to excellent performance of Na-ASSBs, especially at high current rates and during long-term cycling tests at room temperature. Interestingly, heating the  $x = 1.625$  and  $x = 2.000$  compositions induces crystallization and a corresponding redistribution of Na among prismatic and octahedral sites in the structure, resulting in decreased  $\text{Na}^+$  mobility. This finding further highlights the importance of controlling sample crystallinity and the distribution of Na local environments, suggesting that small grain sizes and fast  $\text{Na}^+$  hopping between prismatic environments are key for achieving high conductivity in this class of materials. This work provides insights into the composition, structure, and conductivity relationships of nanocrystalline and amorphous chlorides, which may be used as design principles and that could lead to a paradigm shift in the development of future  $\text{Li}^+$  and  $\text{Na}^+$  conductors for high-performance room temperature ASSBs.

## EXPERIMENTAL PROCEDURES

### Resource availability

#### Lead contact

Further information and requests for resources should be directed to and will be fulfilled by the lead contact, Y. Shirley Meng ([shirleymeng@uchicago.edu](mailto:shirleymeng@uchicago.edu)).

### Materials availability

This study did not generate new, unique reagents.

### Data and code availability

Requests for the data and code utilized in this work will be handled by the lead contact, Y. Shirley Meng ([shirleymeng@uchicago.edu](mailto:shirleymeng@uchicago.edu)).

### Sample preparation

All materials were synthesized under an inert Ar atmosphere. NaCl (Sigma-Aldrich, 99%), YCl<sub>3</sub> (Sigma-Aldrich, 99.9%), and ZrCl<sub>4</sub> (Sigma-Aldrich, 99.9%) anhydrous powders were used as received from the materials vendor. Mechanochemical synthesis was carried out using a high-energy Retsch E<sub>MAX</sub> ball mill, where a 30:1 mass ratio of 5 mm yttrium-stabilized zirconia grinding media to precursor powder was used. 1 g of stoichiometric amounts of Na<sub>2.25-x</sub>Y<sub>0.25</sub>Zr<sub>0.75</sub>Cl<sub>6-x</sub> (where x = 1.375, 1.5, 1.625, 1.75, 1.875, and 2) powders were prepared by hand mixing the precursor powders with a mortar and pestle before loading the powders into the milling jars, which were hermetically sealed in the glovebox. Samples were ball milled at 500 RPM for a total of 5 h.

The Na<sub>0.625</sub>Y<sub>0.25</sub>Zr<sub>0.75</sub>Cl<sub>4.375</sub> (x = 1.625) and Na<sub>0.25</sub>Y<sub>0.25</sub>Zr<sub>0.75</sub>Cl<sub>4</sub> (x = 2.000) compositions were subjected to heat treatments to induce crystallization. The powders were cold pressed into pellets, loaded into quartz ampoules, and then flame sealed under a vacuum. The pelletized samples were heated at 100°C for a duration of 2 h.

Na<sub>2</sub>(B<sub>12</sub>H<sub>12</sub>)<sub>0.5</sub>(B<sub>10</sub>H<sub>10</sub>)<sub>0.5</sub> powders were prepared by ball milling a stoichiometric ratio Na<sub>2</sub>B<sub>10</sub>H<sub>10</sub> (Boron Specialties) and Na<sub>2</sub>B<sub>12</sub>H<sub>12</sub> (Boron Specialties) precursor powders together for a total of 2 h at 500 rpm. The SE powder was collected and subsequently dried under vacuum at 175°C for 48 h.

### X-ray diffraction measurements

XRD patterns were collected over a 5°–50° 2θ range with a step size of 0.01° using a Bruker X8-ApexII CCD Sealed Tube diffractometer equipped with a molybdenum source radiation (λ<sub>Mo</sub> = 0.7107 Å). All samples were hermetically sealed in 0.5-mm-diameter boron-rich capillary tubes.

### Scanning and transmission electron microscopy imaging

SEM images were collected using an FEI Scios DualBeam FIB, equipped with an Everhart–Thornley Detector. TEM characterization was carried out on a Talos F200X scanning/transmission electron microscope with an accelerating voltage of 200 kV. The microscope is equipped with a CETA camera and a low-dose system. The SAED images were acquired with an electron dose rate of ~0.05 e<sup>-</sup> Å<sup>-2</sup> s<sup>-1</sup> for ~8 s.

### Nuclear magnetic resonance measurements

<sup>23</sup>Na measurements were carried out using a 3.2-mm HX probe and a Bruker Advance III Ultrashield Plus 800 MHz spectrometer, equipped with an 18.8-T wide-bore magnet (operating at the Larmor frequency of 132.3 MHz for <sup>23</sup>Na). Experiments were performed using a 3.2-mm MAS probe with a 12-kHz MAS rate. All samples were packed inside an Ar-filled glovebox to avoid direct contact with moisture in the ambient atmosphere. Room temperature spectra were collected on the various Na<sub>2.25-x</sub>Y<sub>0.25</sub>Zr<sub>0.75</sub>Cl<sub>6-x</sub> compositions, with x = 1.375, 1.5, 1.625, 1.75, 1.875, and 2.000. Moreover, room temperature spectra were also collected on x = 1.625 and 2.000 samples heat treated at 100°C. A single pulse length of 0.29 μs at 200 W corresponding to a π/6 excitation pulse with a recycle delay of

10 s was used for all acquisitions. Given the quadrupolar nature of  $^{23}\text{Na}$ , pulses with a  $\pi/6$  flip angle were leveraged to uniformly excite all resonances. All  $^{23}\text{Na}$  NMR shifts were referenced relative to a 1 M aqueous solution of NaCl. The data were processed and extracted using Topspin and ssNake software,<sup>44</sup> respectively.

### Conductivity measurements

The SEs' ionic conductivities were extracted from EIS measurements. C|SE|C cells were assembled using a 10-mm-diameter polyether ether ketone die, where SE pellets were formed by cold pressing 100 mg of SE powder at a pressure of  $\sim 300$  MPa. The EIS data were acquired using a Biologic SP-200 impedance analyzer with a sinusoidal amplitude of 10 mV within a frequency range of 7 MHz to 1 Hz. Activation energies were determined via regression of the linearized Arrhenius plot:  $\ln(\sigma T) \propto 1/T$ .

The SEs' electronic conductivity was determined using the direct current polarization method by applying a bias of 50 mV over 900 s and extracting the steady-state leakage current.

### Electrochemical measurements

Linear sweep voltammetry was conducted using the following cell configuration:  $\text{Na}_9\text{Sn}_4|\text{NBH}|\text{chloride SE}|\text{chloride SE composite}$ . The positive electrode composite consisted of 80 wt % chloride SE and 20 wt % acetylene black (AB) conductive additive, which was added to ensure electronic percolation within the composite to accurately assess its redox processes.

Electrochemical performance was tested with the cell configuration  $\text{Na}_9\text{Sn}_4|\text{NBH}|\text{cathode composite}$  with the respective amounts of 35, 50, and 16.54 mg of each material. The cathode composites were composed of  $\text{NaCrO}_2$ ,  $\text{Na}_{2.25-x}\text{Y}_{0.25}\text{Zr}_{0.75}\text{Cl}_{6-x}$  (where  $x = 1.625$  or 2), and vapor-grown carbon fiber conductive additive in a weight ratio of 11:16:0.5. Constant current cycling of the fabricated cells was carried out at an ambient temperature of approximately 23°C, within the voltage range of 1.7–3.4 V versus  $\text{Na}_9\text{Sn}_4$ , and under an applied stack pressure of  $\sim 50$ –70 MPa.

### SUPPLEMENTAL INFORMATION

Supplemental information can be found online at <https://doi.org/10.1016/j.matt.2023.12.028>.

### ACKNOWLEDGMENTS

P.R. acknowledges Corning Inc. for having supported his Ph.D. research through the Corning Glass Age Scholarship. Funding to support this work was provided by the National Science Foundation through the Partnerships for Innovation (PFI) grant no. 2044465. Characterization work was performed in part at the San Diego Nanotechnology Infrastructure (SDNI), a member of the National Nanotechnology Coordinated Infrastructure, which is supported by the National Science Foundation under grant ECCS-1542148. This work made use of the shared facilities of the UC Santa Barbara MRSEC (grant DMR 1720256), a member of the Materials Research Facilities Network (<http://www.mrfn.org>). The authors would also like to acknowledge the UCSD Crystallography Facility.

### AUTHOR CONTRIBUTIONS

Conceptualization, P.R.; investigation, P.R., E.S., G.D., Y.-T.C., B.S., A.C., G.D., and S.-Y.H.; data curation, P.R., D.H.S.T., J.M.D., J.A.S.O., and J.J.; writing – original

draft, P.R.; writing – review & editing, L.H.B.N., E.S., J.A.S.O., E.A.W., J.J., and R.C.; formal analysis, P.R. L.H.B.N., E.S., and J.J.; funding acquisition: Y.S.M.

## DECLARATION OF INTERESTS

The authors declare no competing interests.

Received: June 6, 2023

Revised: September 19, 2023

Accepted: December 18, 2023

Published: January 18, 2024

## REFERENCES

- Yang, H.-L., Zhang, B.-W., Konstantinov, K., Wang, Y.-X., Liu, H.-K., and Dou, S.-X. (2021). Progress and Challenges for All-Solid-State Sodium Batteries. *Adv. Energy and Sustain. Res.* 2, 2000057.
- Hirsh, H.S., Li, Y., Tan, D.H.S., Zhang, M., Zhao, E., and Meng, Y.S. (2020). Sodium-Ion Batteries Paving the Way for Grid Energy Storage. *Adv. Energy Mater.* 10, 2001274.
- Sayahpour, B., Hirsh, H., Parab, S., Nguyen, L.H.B., Zhang, M., and Meng, Y.S. (2022). Perspective: Design of cathode materials for sustainable sodium-ion batteries. *MRS Energy Sustain.* 9, 183–197.
- Wu, E.A., Banerjee, S., Tang, H., Richardson, P.M., Doux, J.-M., Qi, J., Zhu, Z., Grenier, A., Li, Y., Zhao, E., et al. (2021). A stable cathode-solid electrolyte composite for high-voltage, long-cycle-life solid-state sodium-ion batteries. *Nat. Commun.* 12, 1256.
- Kato, Y., Hori, S., Saito, T., Suzuki, K., Hirayama, M., Mitsui, A., Yonemura, M., Iba, H., and Kanno, R. (2016). High-power all-solid-state batteries using sulfide superionic conductors. *Nat. Energy* 1, 16030–16037.
- Yamane, H., Shibata, M., Shimane, Y., Junke, T., Seino, Y., Adams, S., Minami, K., Hayashi, A., and Tatsumisago, M. (2007). Crystal structure of a superionic conductor. *Solid State Ion.* 178, 1163–1167.
- Kamaya, N., Homma, K., Yamakawa, Y., Hirayama, M., Kanno, R., Yonemura, M., Kamiyama, T., Kato, Y., Hama, S., Kawamoto, K., and Mitsui, A. (2011). A lithium superionic conductor. *Nat. Mater.* 10, 682–686.
- Hayashi, A., Noi, K., Sakuda, A., and Tatsumisago, M. (2012). Superionic glass-ceramic electrolytes for room-temperature rechargeable sodium batteries. *Nat. Commun.* 3, 856.
- Hayashi, A., Masuzawa, N., Yubuchi, S., Tsuji, F., Hotehama, C., Sakuda, A., and Tatsumisago, M. (2019). A sodium-ion sulfide solid electrolyte with unprecedented conductivity at room temperature. *Nat. Commun.* 10, 5266.
- Song, S., Duong, H.M., Korsunsky, A.M., Hu, N., and Lu, L. (2016). A Na<sup>+</sup> Superionic Conductor for Room-Temperature Sodium Batteries. *Sci. Rep.* 6, 32330.
- Liu, Y., Sun, Q., Wang, D., Adair, K., Liang, J., and Sun, X. (2018). Development of the cold sintering process and its application in solid-state lithium batteries. *J. Power Sources* 393, 193–203.
- Ke, X., Wang, Y., Ren, G., and Yuan, C. (2020). Towards rational mechanical design of inorganic solid electrolytes for all-solid-state lithium ion batteries. *Energy Storage Mater.* 26, 313–324.
- Wenzel, S., Leichtweiss, T., Weber, D.A., Sann, J., Zeier, W.G., and Janek, J. (2016). Interfacial Reactivity Benchmarking of the Sodium Ion Conductors Na<sub>3</sub>PS<sub>4</sub> and Sodium β-Alumina for Protected Sodium Metal Anodes and Sodium All-Solid-State Batteries. *ACS Appl. Mater. Interfaces* 8, 28216–28224.
- Culver, S.P., Koerver, R., Zeier, W.G., and Janek, J. (2019). On the Functionality of Coatings for Cathode Active Materials in Thiophosphate-Based All-Solid-State Batteries. *Adv. Energy Mater.* 9, 1900626.
- Han, Y., Jung, S.H., Kwak, H., Jun, S., Kwak, H.H., Lee, J.H., Hong, S.-T., and Jung, Y.S. (2021). Single- or Poly-Crystalline Ni-Rich Layered Cathode, Sulfide or Halide Solid Electrolyte: Which Will be the Winners for All-Solid-State Batteries? *Adv. Energy Mater.* 11, 2100126.
- Asano, T., Sakai, A., Ouchi, S., Sakaida, M., Miyazaki, A., and Hasegawa, S. (2018). Solid Halide Electrolytes with High Lithium-Ion Conductivity for Application in 4 V Class Bulk-Type All-Solid-State Batteries. *Adv. Mater.* 30, 1803075.
- Li, X., Liang, J., Luo, J., Norouzi Banis, M., Wang, C., Li, W., Deng, S., Yu, C., Zhao, F., Hu, Y., et al. (2019). Air-stable Li<sub>3</sub>InCl<sub>6</sub> electrolyte with high voltage compatibility for all-solid-state batteries. *Energy Environ. Sci.* 12, 2665–2671.
- Park, K.-H., Kaup, K., Assoud, A., Zhang, Q., Wu, X., and Nazar, L.F. (2020). High-Voltage Superionic Halide Solid Electrolytes for All-Solid-State Li-Ion Batteries. *ACS Energy Lett.* 5, 533–539.
- Kwak, H., Han, D., Lyoo, J., Park, J., Jung, S.H., Han, Y., Kwon, G., Kim, H., Hong, S.-T., Nam, K.-W., and Jung, Y.S. (2021). New Cost-Effective Halide Solid Electrolytes for All-Solid-State Batteries: Mechanochemically Prepared Fe<sup>3+</sup>-Substituted Li<sub>2</sub>ZrCl<sub>6</sub>. *Adv. Energy Mater.* 11, 203190.
- Kim, S.Y., Kaup, K., Park, K.-H., Assoud, A., Zhou, L., Liu, J., Wu, X., and Nazar, L.F. (2021). Lithium Ytterbium-Based Halide Solid Electrolytes for High Voltage All-Solid-State Batteries. *ACS Mater. Lett.* 3, 930–938.
- Zhou, L., Zuo, T.-T., Kwok, C.Y., Kim, S.Y., Assoud, A., Zhang, Q., Janek, J., and Nazar, L.F. (2022). High areal capacity, long cycle life 4 V ceramic all-solid-state Li-ion batteries enabled by chloride solid electrolytes. *Nat. Energy* 7, 83–93.
- Sebti, E., Evans, H.A., Chen, H., Richardson, P.M., White, K.M., Giovine, R., Koirala, K.P., Xu, Y., Gonzalez-Corraea, E., Wang, C., et al. (2022). Stacking Faults Assist Lithium-Ion Conduction in a Halide-Based Superionic Conductor. *J. Am. Chem. Soc.* 144, 5795–5811.
- Schlem, R., Banik, A., Eckardt, M., Zobel, M., and Zeier, W.G. (2020). Na<sub>3-x</sub>Er<sub>1-x</sub>Zr<sub>x</sub>Cl<sub>6</sub>—A Halide-Based Fast Sodium-Ion Conductor with Vacancy-Driven Ionic Transport. *ACS Appl. Energy Mater.* 3, 10164–10173.
- Liang, J., Li, X., Wang, S., Adair, K.R., Li, W., Zhao, Y., Wang, C., Hu, Y., Zhang, L., Zhao, S., et al. (2020). Site-Occupation-Tuned Superionic Li<sub>x</sub>ScCl<sub>3+x</sub>Halide Solid Electrolytes for All-Solid-State Batteries. *J. Am. Chem. Soc.* 142, 7012–7022.
- Park, D., Kim, K., Chun, G.H., Wood, B.C., Shim, J.H., and Yu, S. (2021). Materials design of sodium chloride solid electrolytes Na<sub>3</sub>MCl<sub>6</sub> for all-solid-state sodium-ion batteries. *J. Mater. Chem. A* 9, 23037–23045.
- Qie, Y., Wang, S., Fu, S., Xie, H., Sun, Q., and Jena, P. (2020). Yttrium–Sodium Halides as Promising Solid-State Electrolytes with High Ionic Conductivity and Stability for Na-Ion Batteries. *J. Phys. Chem. Lett.* 8.
- Zhang, K., and Jin, Z. (2022). Halogen-enabled rechargeable batteries: Current advances and future perspectives. *Energy Storage Mater.* 45, 332–369.
- Kwak, H., Lyoo, J., Park, J., Han, Y., Asakura, R., Remhof, A., Battaglia, C., Kim, H., Hong, S.-T., and Jung, Y.S. (2021). Na<sub>2</sub>ZrCl<sub>6</sub> enabling highly stable 3 V all-solid-state Na-ion batteries. *Energy Storage Mater.* 37, 47–54.
- Zhang, Z., Li, H., Kaup, K., Zhou, L., Roy, P.-N., and Nazar, L.F. (2020). Targeting Superionic Conductivity by Turning on Anion Rotation at Room Temperature in Fast Ion Conductors. *Matter* 2, 1667–1684.
- Sebti, E., Qi, J., Richardson, P.M., Ridley, P., Wu, E.A., Banerjee, S., Giovine, R., Cronk, A.,

- Ham, S.-Y., Meng, Y.S., et al. (2022). Synthetic control of structure and conduction properties in Na–Y–Cl solid electrolytes. *J. Mater. Chem. A Mater.* *10*, 21565–21578.
31. Schlem, R., Mui, S., Prinz, N., Banik, A., Shao-Horn, Y., Zobel, M., and Zeier, W.G. (2020). Mechanochemical Synthesis: A Tool to Tune Cation Site Disorder and Ionic Transport Properties of Li<sub>3</sub>MCl<sub>6</sub> (M = Y, Er) Superionic Conductors. *Adv. Energy Mater.* *10*, 1903719.
32. Banik, A., Famprikis, T., Ghidui, M., Ohno, S., Kraft, M.A., and Zeier, W.G. (2021). On the underestimated influence of synthetic conditions in solid ionic conductors. *Chem. Sci.* *12*, 6238–6263.
33. Preishuber-Pflügl, F., and Wilkening, M. (2016). Mechanochemically synthesized fluorides: local structures and ion transport. *Dalton Trans.* *45*, 8675–8687.
34. Berbano, S.S., Seo, I., Bischoff, C.M., Schuller, K.E., and Martin, S.W. (2012). Formation and structure of Na<sub>2</sub>S+P<sub>2</sub>S<sub>5</sub> amorphous materials prepared by melt-quenching and mechanical milling. *J. Non-Cryst. Solids* *358*, 93–98.
35. Harris, R.K., and Nesbitt, G.J. (1988). Cross polarization for quadrupolar nuclei—Proton to sodium-23. *J. Magn. Reson.* *78*, 245–256.
36. Levitt, M.H. (2013). *Spin Dynamics: Basics of Nuclear Magnetic Resonance* (John Wiley & Sons).
37. Nguyen, H., Banerjee, A., Wang, X., Tan, D., Wu, E.A., Doux, J.-M., Stephens, R., Verbist, G., and Meng, Y.S. (2019). Single-step synthesis of highly conductive Na<sub>3</sub>PS<sub>4</sub> solid electrolyte for sodium all solid-state batteries. *J. Power Sources* *435*, 126623.
38. Kaup, K., Bazak, J.D., Vajargah, S.H., Wu, X., Kulisch, J., Goward, G.R., and Nazar, L.F. (2020). A Lithium Oxythioborosilicate Solid Electrolyte Glass with Superionic Conductivity. *Adv. Energy Mater.* *10*, 1902783.
39. Bamford, D., Reiche, A., Dlubek, G., Alloin, F., Sanchez, J.-Y., and Alam, M.A. (2003). Ionic conductivity, glass transition, and local free volume in poly(ethylene oxide) electrolytes: Single and mixed ion conductors. *J. Chem. Phys.* *118*, 9420–9432.
40. Swenson, J., and Börjesson, L. (1996). Correlation between Free Volume and Ionic Conductivity in Fast Ion Conducting Glasses. *Phys. Rev. Lett.* *77*, 3569–3572.
41. Smith, J.G., and Siegel, D.J. (2020). Low-temperature paddlewheel effect in glassy solid electrolytes. *Nat. Commun.* *11*, 1483.
42. Deysler, G., Chen, Y.-T., Sayahpour, B., Lin, S.W.-H., Ham, S.-Y., Ridley, P., Cronk, A., Wu, E.A., Tan, D.H.S., Doux, J.-M., et al. (2022). Evaluating Electrolyte–Anode Interface Stability in Sodium All-Solid-State Batteries. *ACS Appl. Mater. Interfaces* *14*, 47706–47715.
43. Sakuda, A., Hayashi, A., and Tatsumisago, M. (2013). Sulfide Solid Electrolyte with Favorable Mechanical Property for All-Solid-State Lithium Battery. *Sci. Rep.* *3*, 2261.
44. van Meerten, S.G.J., Franssen, W.M.J., and Kentgens, A.P.M. (2019). ssNake: A cross-platform open-source NMR data processing and fitting application. *J. Magn. Reson.* *301*, 56–66.